Activating a Semiconductor-Liquid Junction via Laser-Derived Dual Interfacial Layers for Boosted Photoelectrochemical Water Splitting

Jie Jian[1], Qian Ye[1], Fan Li[1], Guirong Su[2], Wei Liu[2], Changzhen Qu[1], Can Li[3], Lichao Jia[3], Andrei Novikov [4], Vladimir A. Vinokurov[4], Daniel H. S. Harvey[5], Dmitry Shchukin[5], Dennis Friedrich[6], Roel van de Krol[6], and Hongqiang Wang[1]

Affiliation:

1. State Key Laboratory of Solidification Processing, Center for Nano Energy Materials, School of Materials Science and Engineering, Northwestern Polytechnical University and Shaanxi Joint Labortary of Graphene, Xi'an, 710072, P. R. China.
2. Nano and Heterogeneous Materials Center, School of Materials Science and Engineering, Nanjing University of Science and Technology, Nanjing 210094, Jiangsu, China.
3. Key Laboratory of Applied Surface and Colloid Chemistry, National Ministry of Education, Shaanxi Key Laboratory for Advanced Energy Devices, Shaanxi Engineering Lab for Advanced Energy Technology, School of Materials Science and Engineering, Institution Shaanxi Normal University, Address 2620 West Chang'an Street, Xi'an, Shaanxi, 710119, China.
4. Gubkin Russian State University of Oil and Gas, Gubkin University, 19991, Moscow, 65/1 Leninsky prospect, Russia.
5. Stephenson Institute for Renewable Energy, University of Liverpool, Liverpool L69 7ZF, UK.
6. Institute for Solar Fuels, Helmholtz-Zentrum Berlin für Materialien und Energie GmbH, Hahn-Meitner-Platz 1,14109 Berlin, Germany Institution.

Key words: pulsed laser irradiation; carbon dots; phenolic hydroxyl groups; $BiVO_4$ photoanode; PEC water splitting

Abstract:

Developing viable photoelectrochemical water splitting requires tackling the sluggish interfacial charge carrier dynamics and kinetically suppressed photo-corrosion of the metal oxide photoelectrodes; furthermore, a great challenge remains in developing the semiconductor-liquid junction (SCLJ) with synchronously boosted photoelectrochemical activity and operational stability. Demonstrated herein is a strategy of creating an active and stable SCLJ with a unique configuration of dual interfacial layers at the surface of the $BiVO_4$ photoanode, derived from the grafting of laser generated carbon dots (LGCDs) with rationally designed functional groups. The dual interfacial layers were experimentally verified effective, not only to activate respectively the carrier transport and transfer in each dual layer, but in boosting the operational stability of the photoanode. This is owing to the improved charge dynamics and the uniform covalent coating of LGCDs, yielding a $BiVO_4$ photoanode with charge injection efficiency (η_{inj}) of up to 92.44%, a photocurrent density of 6.08 mA cm^{-2} @ 1.23 V_{RHE}, as well as pronounced operational stability of 120 hours @ 1.23 V_{RHE}. Such laser-matter reaction-based strategy was further found generally useful to create an effective SCLJ with boosted photoelectrochemical activity and stability that bother most of the metal oxides based photoelectrodes.

1. Introduction

Photoelectrochemical (PEC) water splitting is an important alternative to produce nature-benign, sustainable hydrogen[1, 2]. Affordable and highly durable metal oxides semiconductors (MOSs), used as photoelectrodes to produce and migrate photo-generated charge carriers to the semiconductor-liquid junction (SCLJ) for energy storage reactions, have been the subject of intensive research[3-6]. In addressing the intrinsic sluggish charge carrier dynamics in the bulk owing to the covalent bonding nature of MOSs[7-8], the past decade has witnessed the great potentials of a series of MOSs for high performance photoelectrochemical water splitting, through huge efforts dedicated to nano-structuring[9], crystal facet engineering[10], compositional tuning[11], intrinsic defects modulation[12], doping[13], and nanocrystals embedding[14]. Challenges still remain on modulating the SCLJ[15-16], which is the dominant place where both charge transfer and energy storage reactions occur. Engineering improvements to the SCLJ would have a significant impact on the interfacial charge separation and transfer, as well as the operational stability that is kinetically controlled by the rate of photo-corrosion with that of the interfacial charge transfer and/or surface recombination. Developing engineering protocols at the SCLJ to activate the interfacial carrier dynamics and boost the operational stability is thus of great significance for viable hydrogen generation through MOS based photoelectrodes.

To create MOS based photoelectrodes that are both photoelectrochemically active and have stable surfaces, a variety of co-catalysts with the ability of increasing interfacial charge transfer rate and inhibiting surface photo-corrosion[17-18] (such as Co-Pi and Fe/Ni (oxy)hydroxides)[19-21] have been developed. The dual-layer of FeOOH/NiOOH oxygen evolution catalysts developed by Choi's group showed effective reduction of interfacial charge recombination at the SCLJ, resulting in pronounced 48 h operational stability @ 0.6 V_{RHE}[20]. Moreover, a series of stable metal oxides (such as NiO and Co_3O_4)[15, 22] have been adopted to facilitate interfacial carriers transfer at the SCLJ by forming heterojunctions. This triggered the recent efforts on physically depositing a variety of low-dimensional materials including black phosphorus[23-24], MXenes[25] and carbon dots[26] on MOS based photoelectrodes by virtue of their advances in conductivity and band alignment that facilitate the charge transfer[27-28].

The creation of intrinsic oxygen vacancies at MOSs surface via aqueous treatment[29], plasma treatment[30], photoetching[31], and photo-polarizing[32] has highlighted the significance of surface modulation through the creation of a shallow intrinsic defective energy level. This provides potential

for the charge carrier concentration and conductivity to be significantly boosted, resulting in accelerated interfacial charge carrier separation and transfer, thus promoted PEC performance. All these endeavors manifest that it would be highly promising to advance PEC water splitting through the creation of an effective surface of photoelectrodes with synchronously boosted charge carrier transport/transfer and kinetically suppressed photo-corrosion, at the SCLJ. This is not without its own challenge of the technical hurdle of simultaneously overlaying the two advantages at the surface of MOSs based photoelectrodes.

An effective strategy of creating $BiVO_4$ top surfaces with the unique configuration of dual interfacial layers to synchronously boost the PEC activity and stability of the photoanodes, via grafting laser generated carbon dots with phenolic hydroxyl groups (LGCDs-PHGs), is presented. The simple soaking of the prepared Mo-$BiVO_4$ (MBVO) photoelectrodes in a colloidal solution of LGCDs-PHGs, accessed via pulsed laser treatment of tannic acid (TA) in acetone, yields simultaneously dual interfacial layers comprising of the grafted LGCDs-PHGs layer and MBVO with rich oxygen vacancies (MBVO-V_O) layer, is schematically demonstrated in **Scheme 1a**. The bespoke configuration of dual interfacial layers can improve both the PEC performance and the long-term operational stability; the MBVO-V_O layer can activate the charge carrier dynamics for accelerating charge transport and reducing charge accumulation, while the LGCDs-PHGs layer can both promote the hole extraction and form the uniform coating layer for inhibiting the photo-corrosion of the film (**Scheme 1b**). The construction of dual interfacial layers resulted in an increased photocurrent density of MBVO up to 6.08 mA cm^{-2}, with a dual-photoanode configuration and an enhanced charge injection efficiency (η_{inj}) of 92.44% @ 1.23 V_{RHE}. Moreover, the LGCDs-PHGs-MBVO photoanode showed a greatly enhanced operational stability up to 120 h at 1.23 V_{RHE}, a value among the top in the stability records of $BiVO_4$ based photoanodes (**Table S3**). This pronounced stability was experimentally verified and related with not only the uniform covalent coating of the LGCDs for suppressed photo-corrosion, but also the accelerated charge transfer at the top layer of LGCDs-PHGs, and the improved charge transport at the shallow MBVO-V_O layer. Further work exploring LGCDs with other grafting functional groups by pulsed laser irradiation of catecholic compounds determined that the methodology to boost the PEC behavior of MBVO is not restricted to the compounds explored initially. As such it is proposed that this methodology provides an effective alternative for addressing interfacial carrier dynamics and operational stability issues in MOS photoelectrodes.

2. Results

2.1 Laser Generated Carbon Dots with Phenolic Hydroxyl Groups (LGCDs-PHGs)

Figure S1a depicts the generation of LGCDs-PHGs via the technique of pulsed Laser Synthesis and Processing of Colloids (LSPC) that has been attractive to create metastable nanomaterials due to the required, extreme, non-equilibrium conditions[33-37]. Typically, 20 mg TA (with flocculent morphology and polyhydroxy phenolic structure, **Figure S2**) is uniformly dispersed in 10 mL acetone by ultrasonication, and then subjected to the irradiation of an unfocused pulsed laser beam with a laser fluence of 850 mJ $pulse^{-1}$ cm^{-2} (repetition rate 10 Hz; third harmonic) for 8 minutes. The resulting solution turns light yellow from the initial transparent (insert of **Figure S1a**), and demonstrates apparent Tyndall scattering, indicating the generation of colloidal particles (bottom left insert of **Figure 1a**). Transmission Electron Microscopy (TEM) analysis shown in **Figure 1a** demonstrates that the laser generated nano-colloids have an average size of 2.6 nm. The high-resolution TEM (HRTEM) analysis shown in **Figure 1b** shows an interlayer space of ~0.208 nm, corresponding to the (103) lattice fringe of graphite (PDF card number: 26-1083). Raman spectroscopy characterization (**Figure 1c**) of the colloidal particles shows the typical peaks at 1366 and 1588 cm^{-1}, which corresponds to the D and G bands of the graphite carbon, respectively. The correlated signal intensity ratio of the D-band and G-band (I_D/I_G) is ~0.69, indicating that these carbons retain good crystallinity, consistent with the HRTEM analysis. The colloidal solution exhibits excitation wavelength-dependent photoluminescence (PL) (**Figure S3a)** and shows enhanced optical absorption (**Figure S3b)** compared to that of the original TA solution. These results suggest that laser generated carbons dots with homogeneous size can be synthesized via the simple pulsed laser irradiation of catecholic solution. A hypothesis drawn from these results is that the instantaneous alternative heating and quenching involved in pulsed laser treatment is capable of transforming the fully chained benzene ring of TA into graphitic carbon dots; through polymerization, carbonization and graphitization successively occurring between pulses (**Figure S4**)[37], leaving numerous phenolic hydroxyl groups on carbon surfaces (**Figures 1a-c** and **S5**).

X-ray photoelectron spectroscopy (XPS) measurements were further adopted to clarify the surface chemical state of carbon dots (**Figure S6** and **Table S1**). The deconvolution results demonstrate that the peaks of high-resolution C 1s spectra located at 284.6, 286.3, 288.9 and 291.5 eV can be identified respectively as C-C, C-OH, O-C=O and π-π* shake-up satellite, as shown in **Figure 1d**[38-39]. It is clear that the hydroxyl groups were observed in the carbon dots, and the intensity of π-π* shake-up satellite dramatically declined following laser irradiation (**Figure S6c** and **Table S2**). This indicates

that the formation of carbon dots is a result of the reconstruction of the carbon framework from the benzene ring in TA[37], while the functionalized groups of phenolic hydroxyls have been inherited. Such laser generated carbon dots with phenolic hydroxyl groups (LGCDs-PHGs) are stable due to the phenolic hydroxyls on the surface, which inhibit agglomeration of the LGCDs-PHGs and guarantee stability for over 3 months (**Figure S7**).

2.2 Interfacial Layer of LGCDs-PHGs on MBVO Films

The functional group of phenolic hydroxyls has been reported beneficial for the coordination with diverse metal ions[40-42], and exploration of the effects of grafting LGCDs-PHGs on MBVO films was subsequently investigated. Following MBVO films fabrication [14], LGCDs-PHGs were grafted on to MBVO by simply soaking the MBVO films in LGCDs-PHGs colloidal solution (**Figure S8**). The LGCDs-PHGs-MBVO film shows worm-like nanoporous structure with an average diameter of ~200 nm and a thickness of ~250 nm (**Figures S9b and S9d**), which is similar with that of the films without grafting (**Figures S9a and S9c**). The grafting shows little influence on the crystal structure and optical absorbance of the MBVO films (**Figures S10, S11 and S12**), while the backscattered scanning electron microscopy (BSE) implies the atomic number contrast presents an obvious difference between films of MBVO and LGCDs-PHGs-MBVO films. The black dots that represent the lower atomic weights of C can be observed distributed all over the surface of LGCDs-PHGs-MBVO (**Figure 1f)**, while the MBVO film (**Figure 1e**) shows no significant difference throughout the entire surface. Despite the grafting having little optical or structural impact, the contact angle was decreased from 48.7° for the MBVO film (**Figure 1g**) to 20.5° for the LGCDs-PHGs-MBVO film (**Figure 1h**); this is a result of the successful grafting of LGCDs-PHGs on MBVO and is owing to the hydrophilic nature of the phenolic hydroxyl groups. Such increased hydrophilicity could facilitate the adsorption of water molecules onto the active site of LGCDs-PHGs-MBVO film in the application of water splitting.

The existence of the LGCDs-PHGs on the MBVO surface was further confirmed by TEM analysis of the LGCDs-PHGs-MBVO film. **Figures 1i** and **S14a**, show a uniform and fully covered thin layer, with thickness of ~4 nm, on the LGCDs-PHGs-MBVO surface, compared with that of the MBVO film (**Figure S13**). The HRTEM image (**Figures 1j** and **S14b)** reveals the interlayer space of 0.292 nm and 0.467 nm in the matrix, corresponding to the (040) and (011) plane of $BiVO_4$, as well as the existence of carbon dots with d-spacing of 0.213 nm, corresponding to the (102) lattice fringe of graphite (PDF card number: 26-1083); the amorphous section of the thin layer is predicted to be the

phenolic hydroxyl groups that bridge the carbon dots[42]. In addition, transmission electron microscopy energy-dispersive X-ray spectroscopy (TEM-EDS) analysis was carried out to analyze the element distribution of LGCDs-PHGs-MBVO, which further confirms the homogeneous coverage of LGCDs-PHGs (**Figure 1k**), differing from the cases in physical deposition of low dimensional materials[23-26].

X-ray photoelectron spectroscopy (XPS) study of the C 1s spectrum verified the local coordination chemical state of the carbon dots on the LGCDs-PHGs-MBVO film. The C 1s spectrum of LGCDs-PHGs-MBVO shown in **Figure 1l** displays the existence of C-C, C-OH and O-C=O with slight π-π* shake-up satellite bonds, confirming the assembly of phenolic hydroxyl groups on the MBVO films. The Fourier-transform infrared spectroscopy (FTIR) shown in **Figure 1m** demonstrates that the stretching vibration of H-O in pure TA appears at 3375.2 cm^{-1}, while it shifts to 3423.6 cm^{-1} in LGCDs-PHGs-MBVO. The positive shift in wavenumber, and decreased intensity of the peaks, reflects the coordination of the phenolic hydroxyl groups with metal ions in MBVO by means of deprotonation, in agreement with the literature[43-44]. The stretching vibration of C based bonds in the region span from 700 to 1700 cm^{-1} of LGCDs-PHGs-MBVO further implies the grafting of LGCDs-PHGs onto the MBVO[44-45].

2.3 Photoelectrochemical Performance of the MBVO Films upon the Grafting of LGCDs-PHGs

The PEC performances were investigated by measuring the photocurrent density-potential (J-V) curves in 1.0 M potassium phosphate buffer (pH = 7) with and without Na_2SO_3 in a standard three-electrode cell system, using cyclic voltammetry (CV) with a scan rate of 10 mV s^{-1}. The film supported by F:SnO_2 (FTO) glass are front-illuminated by a 500 W Xe lamp equipped with an AM 1.5 G filter (100 mW cm^{-2}). As shown in **Figure 2a**, LGCDs-PHGs-MBVO film (**Figure S15**) exhibits an obvious improvement of photocurrent density up to 5.29 mA cm^{-2} for sulfite oxidation, and an increase from the 3.82 mA cm^{-2} observed for the raw MBVO film at 1.23 V_{RHE}. The LGCDs-PHGs-MBVO film also shows a 0.02 mV negative shift of the onset potential, while the photocurrent density of the MBVO films modified by as-received TA (**Figure 2a**) show almost similar behavior with that of the MBVO film. The photocurrent density histograms of 17 samples of MBVO (standard deviation of 4.1%, **Figure S16**) and 17 samples of LGCDs-PHGs-MBVO films (stand deviation of 5.5%, **Figure S16**) are shown in **Figure 2c**, representing the pronounced effects that grafting the LGCDs-PHGs onto the MBVO film has with regards to improved PEC performance. The LGCDs-PHGs grafted MBVO films reach an average photocurrent density of 4.74 mA cm^{-2} at 1.23 V_{RHE},

while pristine MBVO films are only able to achieve an average photocurrent density of 3.57 mA cm^{-2}. The photocurrent density of MBVO and LGCDs-PHGs-MBVO for water oxidation with and without FeNiOOH (**Figure 2b**) also present the same tendency as those measured in sulfite solution. The photocurrent density increases from the original 1.72 mA cm^{-2} for the MBVO film and 3.17 mA cm^{-2} for the FeNiOOH-MBVO film up to 3.04 mA cm^{-2} for the LGCDs-PHGs-MBVO film and 4.89 mA cm^{-2} for the FeNiOOH-LGCDs-PHGs-MBVO film. Further investigation of the FeNiOOH-LGCDs-PHGs-MBVO film was performed via the assembly of dual photoanodes. Its champion photocurrent density reached 6.08 mA cm^{-2} at 1.23 V_{RHE} (**Figure 2d**), which ranks among the top performers of $BiVO_4$ based photoanodes (**Table S3**). The incident photon-to-current conversion efficiency (IPCE) and absorbed photon-to-current conversion efficiency (APCE) reveal the increase of the photocurrent response and photon-to-current conversion of LGCDs-PHGs-MBVO film in the region between 300 nm and 520 nm compared to that of the MBVO film (**Figure S17**). The IPCE and APCE of LGCDs-PHGs-MBVO film could reach up to 59.5% and 75.4%, while the IPCE and APCE of the MBVO film is below 48% and 58%, respectively.

To ascertain the effects the specific functional groups of carbon dots have on PEC performance of MBVO films, carbon dots without ligands on the surface were generated from laser irradiation of toluene[46]. This yielded ligand-free carbon dots with an average size of 5.2 nm, which were subsequently introduced onto the MBVO surface. As shown in **Figure S18**, the photocurrent density of the MBVO film decorated with such carbon dots shows only slight increase, when compared to that of the control film. It should be noted that the carbon dots generated from toluene show poor size uniformity compared to that of LGCDs-PHGs. These results imply that the specific phenolic hydroxyls groups are of great importance for the improvement for PEC performance of MBVO films, as well as the formation of uniform colloidal carbon dots.

Electrochemical impedance spectroscopy (EIS) was used to gain deeper insight into the electronic properties of the LGCDs-PHGs-MBVO films. By fitting the experimental data (small dots) according to the equivalent circuit model, as shown in **Figure 2e**, it is feasible to obtain from the fitted results (solid line) the smaller R_s (series resistance) and R_{ct} (charge transfer resistance)[47, 48] value of the LGCDs-PHGs-MBVO film (8.05 Ω, 1033 Ω). Comparing these values with those of the MBVO films (31.57 Ω and 1988 Ω, respectively) (**Table S4**), indicates enhanced interfacial charge transfer of the LGCDs-PHGs-MBVO film. Further surface charge injection efficient analysis shows that the LGCDs-PHGs-MBVO achieved an enhanced η_{inj} of 57.26% (from 44.95% for MBVO) and the

FeNiOOH-LGCDs-PHGs-MBVO shows further enhancement with η_{inj} values of 92.44%, resulting from the promotion of surface charge transfer (**Figure 2f**).

Based on the Vienna ab initio simulation package (VASP), density of states (DOS) calculation were conducted to analyze the evolution of the electronic structure of MBVO upon the grafting of LGCDs-PHGs. The calculated valance band maximum (VBM) and conduction band minimum (CBM) of monoclinic MBVO is mainly comprised of O 2p and V 3d orbitals (**Figure S19a** and **Figure S20a**), which is in good agreement with published works[7, 49]. The grafting of LGCDs-PHGs shows apparent influence on the VB electronic structure of MBVO by overlapping the C 2p and hydroxyls hybrid orbital with O 2p orbitals (**Figure 2g** and **Figure S19b**). Simulation of the influence of carbon dots without phenolic hydroxyls on electronic structure of MBVO was also performed, and the results highlighted a smaller impact on VB structure (**Figure S19c**, **Figure S20b** and **Table S5**). These observations indicate that the phenolic hydroxyls on LGCDs-PHGs might be one of the important reasons for the upward of VB position of LGCDs-PHGs-MBVO.

Furthermore, based on the Fritz-Haber-Institute ab initio molecular simulations (FHI-aims),[50] the PBE+vdW^{surf} method was employed to calculate the adsorption configurations of the bistable system of LGCDs-PHGs adsorbed on MBVO. By subtracting the electron density of the isolated LGCDs-PHGs, and that of the clean MBVO surface from the adsorption systems, the electron density difference has been calculated to obtain more insight into the charges interaction between LGCDs-PHGs and MBVO. As shown in **Figure 2h**, the charge rearrangement and the averaged differences in charge density have been illustrated over the x-y plane ($\Delta\rho$) along the z-coordinate. This difference is confirmed through calculation of the total transferred electrons via integrating $\Delta\rho(z)$ from a point on the z-axis in the vacuum, where 0.08 electron is transferred from LGCDs-PHGs to MBVO (**Figure 2i**). To determine the effect of the phenolic hydroxyls on LGCDs-PHGs on the electron density difference of the LGCDs-PHGs-MBVO system, the electron density difference of C-MBVO has been calculated (**Figure S21**), where only 0.02 electron is transferred from C to MBVO. According to both the experimental and computational results, both the carbon dots and the phenolic hydroxyls on the LGCDs-PHGs make a great contribution modulating the interfacial electronic and energy state for boosted charge transfer of LGCDs-PHGs-MBVO film.

The grafting of LGCDs-PHGs onto MBVO clearly improves not only the charge injection efficiency (η_{inj}) but charge separation efficiency (η_{sep}) of the MBVO film (**Figure 2f**). The enhanced η_{sep} (from 59.51% to 79.96%) implies efficient charge transport to the surface of the MBVO

photoanode. Mott-Schottky (MS) results in **Figure S22** were further collected to gain deeper insight into the charge transport of LGCDs-MBVO films, which reveals that LGCD-PHGs does not change the n-type feature of the MBVO film, but results in a more negative flat band potential and shallower slopes, indicating its regulated band structure and increased carrier densities for boosted conductivity of the MBVO film upon the LGCDs-PHGs grafting[31, 48, 51]. It is a general consensus that carbon dots are capable of promoting surface charge transfer when coating them on the photoelectrode[26], while the conductivity of LGCDs-PHGs-MBVO film also shows a pronounced increase, implying that the charge transport dynamics of the LGCDs-PHGs-MBVO film can be improved. It is noteworthy to explore the reason behind the boosted charge transport of the MBVO film upon the grafting of LGCDs.

2.4 Interfacial Layer of MBVO with Rich Oxygen Vacancies (MBVO-V_O)

High-resolution X-ray photoelectron spectroscopy (XPS) analysis was performed to clarify the boosted carrier transport of MBVO. As shown in **Figure 3a** and **Table S6**, the O 1s spectra of MBVO can be deconvoluted into three component peaks corresponding to lattice oxygen (O_L, locating at 529.7 eV), oxygen vacancies (O_V, locating at 530.7 eV) and adsorbed oxygen (O_A, locating at 531.8 eV), respectively[28, 52]. After LGCDs-PHGs grafting, the atomic ratio of oxygen vacancies (O_V) in the LGCDs-PHGs-MBVO film increased when compared to that of the MBVO film (from 27.92% to 32.23%), which could induce the increased carrier density and improved electronic conductivity, consistent with the η_{sep} and Mott-Schottky (MS) results (**Figure S22**). Moreover, the atomic ratio and peak position of adsorbed oxygen (O_A) in the LGCDs-PHGs-MBVO film were greatly enhanced (from 10.45% to 21.21%) and positively shifted (from 531.8 eV to 532.4 eV), which could be attributed to an increase in chemisorbed hydroxyls groups due to the absorption of phenolic hydroxyl groups on the LGCDs-PHGs[52]. In addition, the Bi 4f and V 2p peaks of LGCDs-PHGs-MBVO located at around 159.1 eV and 516.8 eV were shifted to lower binding energy compared to that of MBVO (**Figure 3b** and **Figure S23**), indicating the partial reduction of Bi^{3+} and V^{5+} ions caused by the additional oxygen vacancies, where the electrons bound to the metal ions and oxygen could migrate to oxygen vacancies[51-53]. Further depth profile characterization of O 1s suggests that the O_V exist in the shallow surface region (around 20 nm) of the LGCDs-PHGs-MBVO film (**Figure 3c** and **Table S7**). The above results indicate that the grafting of LGCDs-PHGs by soaking, resulted in an interfacial layer of MBVO with rich oxygen vacancies (MBVO-V_O), providing an explanation for the enhanced charge transport of LGCDs-PHGs-MBVO film[31, 51].

To further investigate the reason behind the creation of the interfacial layer of MBVO-V_O, pH and

electrochemical cyclic voltammetry (CV) analyses of different LGCDs-PHGs colloidal solutions were carried out. It was interesting to find that the pH value of LGCDs-PHGs is much lower than that of original TA, as shown in **Figure 3d**. The pH values decrease with the increasing of the laser fluence, implying higher acidity and easier deprotonation capability for the laser treated colloidal solution. In addition, CV results of different LGCDs-PHGs colloidal solutions shown in **Figure 3e** and **Figure S24** indicates that all the LGCDs-PHGs colloidal solutions treated by different laser fluences show more reducing capacity than that of TA, where the higher laser fluence results in stronger oxidation/reduction peaks. Such increased reducing capability allows for the increased oxygen vacancies when soaking the MBVO film in the LGCDs-PHGs colloidal solution. The above results thus indicate the formation of the dual interfacial layer on the $BiVO_4$ photoanode, comprising of the layers of LGCDs-PHGs and MBVO-Vo, schematically illustrated in **Scheme 1a**. This unique configuration of a dual interfacial layer could thus be the reason behind the improved carrier dynamics, where the LGCDs-PHGs-MBVO layer is responsible for the efficient charge extraction by interfacial layer of LGCDs-PHGs, while the MBVO-Vo layer is responsible for the promoted charge transport.

2.5 The effect of Dual Interfacial Layers on Boosted PEC Activity

Electrochemical cyclic voltammetry (CV), VB-XPS analysis, and ultraviolet photoelectron spectroscopy (UPS) analysis was performed on LGCDs-GPHs and LGCDs-PHGs-MBVO films to further clarify the improved charge carrier dynamics of MBVO films upon the formation of the dual interfacial layers. The energy level of LGCDs-PHGs is determined by CV according to previous reports[27, 54-56]. As shown in **Figure 3e**, the CV curve of LGCDs-PHGs shows noticeable oxidation/reduction peaks, while the original TA before laser treatment shows a flat curve without a single peak across the whole test potential range. It is calculated that the lowest unoccupied molecular orbital (LUMO) level of LGCDs-PHGs estimated from the onset reduction potentials is −3.96 eV (depicting the vacuum level as 0 eV), which is more positive than that of the MBVO (−4.69 eV, calculated from UPS in **Figure S25**). Based on the optical bandgap of LGCDs-PHGs (2.48 eV) (**Figure S26**), the highest occupied molecular orbital (HOMO) value is calculated to be −6.44 eV. Such HOMO level of LGCDs-PHGs is thus beneficial for the hole extraction from MBVO to LGCDs-PHGs of LGCDs-PHGs-MBVO film. Band structure investigation of the LGCDs-PHGs-MBVO film by UPS analysis (**Figure S27**) was further conducted, showing that the Fermi level and VB position of the LGCDs-PHGs-MBVO film (0.11 eV of Fermi level and 2.59 eV of VB position, taking RHE as reference) were shifted upward compared to that of the MBVO film (0.31 eV of Fermi level and

2.71 eV of VB position). The VB-XPS analysis (**Figure S28**) also shows the same upward tendency of VB position, implying an improved interfacial charge carrier dynamics for charge separation and hole-extraction[24, 57, 58] by the dual interfacial layers.

The open-circuit potential (OCP) analyses were performed to identify photovoltage of the MBVO and LGCDs-PHGs-MBVO films, which could imply the band bending related driving force and their work function associated with the quasi-Fermi level, further reflecting the role of the dual interfacial layers[12, 16]. As shown in **Figure S29**, the OCP_{dark} always show relatively positive value, while OCP_{light} always show relatively negative, meaning that the large band upward bending in the dark, and the band flattened by photoexcited charge carriers in the light, respectively. The photovoltage (OCP_{light} - OCP_{dark}) of the LGCDs-PHGs-MBVO film is 0.42 V (**Figure 3g**), which is 0.16 V higher than that of the MBVO film. The higher photovoltage of the LGCDs-PHGs-MBVO film represents an enhanced band bending and higher driving force of PEC reaction than that of the MBVO film, which is determined by its hole quasi-Fermi level and the redox potential of the electrolyte (**Figure 3f**)[15]. The OCP results therefore also suggest enhanced charge carrier dynamics by the dual interfacial layer of the LGCDs-PHGs-MBVO films.

2.6 Dual Interfacial Layers for Boosted PEC Stability

Constructing a protective layer on photoelectrodes is one of the most important approaches for suppressing photo-corrosion and achieving boosted stability. An investigation into the effects of the uniform covalent coating of the LGCDs-PHGs on the stability of MBVO films was warranted, and subsequently evaluated by the J-t measurement of the films of MBVO and LGCDs-PHGs-MBVO performed at 1.23 V_{RHE} in 1.0 M potassium phosphate buffer (pH = 7). As shown in **Figure 3h**, the steady-state photocurrent density of the MBVO film dropped to 58.5% after 120 min. The faded photocurrent density of the MBVO photoanode can be ascribed to the anodic photo-corrosion caused by photoinduced surface-accumulated holes and electrochemical dissolution of V^{5+} in $BiVO_4$[21, 59]. When introducing the dual interfacial layers, the photocurrent density of LGCDs-PHGs-MBVO maintained 87.5%, and further improved to 99.8% when coating the layer of FeNiOOH. As a comparison, the stability of LGCDs-MBVO were further investigated to verify the effect of covalent coating by LGCDs-PHGs (**Figure S30**). MBVO films coated by ligand-free LGCDs showed even worse stability than that of the MBVO film (remains only 46.8%). These results imply the important role of uniform covalent anchoring of LGCDs-PHGs on MBVO films for enhanced stability.

Boosting the carrier dynamics to reduce the charge accumulation and recombination at the SCLJ

could suppress the surface photo-corrosion of MBVO film, among which the accelerated charge transfer by LGCDs-PHGs has been verified by both experimental and computational analysis. It is thus worthwhile to further investigate if the improved charge transport in the interfacial layer of MBVO-V_O plays positive roles on the operational stability of the MBVO film. Films of MBVO grafted by LGCDs-PHGs, but without the interfacial layer of MBVO-V_O, were prepared through directly spin-coating LGCDs-PHGs onto MBVO films. The stability test showed that without creating the shallow MBVO-V_O layer, the photocurrent density of MBVO films with only the interfacial layer of LGCDs-PHGs could maintain 69.1% after 120 min, which is much lower than that of 87.5% of MBVO films with dual interfacial layers, but higher than that of 58.5% for MBVO with no interfacial layer (**Figure 3h**). It can thus be concluded that the shallow MBVO-V_O layer contributes to the stability enhancement of the MBVO film, proposedly through the enhanced charge transport which eliminates the charge carriers accumulating on the surface, before they participate in the OER process.

The long-term stability of the FeNiOOH-LGCDs-PHGs-MBVO photoanode was investigated at 1.23 V_{RHE}. As shown in **Figure 3i**, the photocurrent density of the FeNiOOH-LGCDs-PHGs-MBVO photoanode was stable for 120 h without any obvious dropping, which is among the top in the stability records of $BiVO_4$ based photoanodes at 1.23 V_{RHE} (**Table S9**). To further explore the role of the dual interfacial layer for the stability of LGCDs-PHGs-MBVO film, the inductively coupled plasma optical emission spectrometry (ICP-OES) was conducted on the electrolytes used for the J-t measurement (inset of **Figure 3i**). The ICP-OES results suggested the presence of both Bi and V in the three electrolytes after the J-t measurement. The concentration of Bi and V in the electrolyte of the FeNiOOH-LGCDs-PHGs-MBVO and LGCDs-PHGs-MBVO films is significantly lower than that of the MBVO film, and the concentration of Fe and Ni in the electrolyte of the FeNiOOH-LGCDs-PHGs-MBVO also decreases compared to that of the FeNiOOH-MBVO film, indicating efficient suppression of photo-corrosion on the LGCDs-PHGs-MBVO by the dual interfacial layers resulting in pronounced stability. Such pronounced stability was thus considered related with not only the uniform covalent coating of the LGCDs for suppressed photo-corrosion, but also the accelerated charge transfer at the top layer of the LGCDs-PHGs, and the improved charge transport at the shallow MBVO-V_O layer.

2.7 Discussion

Results indicate that laser treated TA-like catecholic molecules can generate LGCDs-PHGs to boost MBVO photoelectrochemical performance. LGCDs-PHGs were similarly prepared from

epigallocatechin gallate (EG) and catechol powders through one-step pulsed laser irradiation, and then coated onto the MBVO photoanode. LGCDs-PHGs colloidal solution can be similarly obtained from EG and catechol (**Figure 4a**, **Figure 4h**, **Figure S31** and **Figure S32**) by pulsed laser irradiation. The TEM analysis shown in **Figure 4b** and **Figure 4i** demonstrates that the LGCDs-PHGs have an average size of 1.91 and 2.00 nm, respectively. The HRTEM analysis shown in inset of **Figure 4b** and **Figure 4i** shows an interlayer space of about 0.213 nm and 0.208 nm, corresponding to the (102) and (103) lattice fringe of graphite (PDF card number: 26-1083), respectively. The C-V and pH results (**Figures 4c-d** and **Figures 4j-k**) show similar oxidation/reduction peaks and energy level, implying the similar easier deprotonation capability and band alignment promotion. The photoelectrochemical measurements (**Figures 4e** and **Figures 4l**) revealed that grafting LGCDs-PHGs from EG and catechol on the MBVO film could also lead to the enhancement of photocurrent density up to 4.62 and 4.35 mA cm^{-2} at 1.23 V_{RHE}, respectively, which could be related to the different structure of raw powders. The enhanced photovoltage (**Figure 4f**, **Figure 4m**, **Figures S33**-**S34**) representing enhanced driving force, and the upward tendency of VB position (**Figure 4g**, **Figure 4n**, **Figures S35**-**S36**) representing more efficient band bending, have been also observed. These results show that LGCDs-PHGs colloidal solutions from different catecholic molecules could always modulate MBVO performance by simply creating the dual interfacial layers.

3. Conclusion

In summary, this work has demonstrated an efficient strategy of addressing the interfacial charge carrier dynamics and operational stability at the SCLJ. Grafting laser generated carbon dots with anchoring functional groups onto MBVO photoanodes has yielded a unique configuration of dual interfacial layers on the surface. Both the experimental and computational results confirm that it is the dual interfacial layers that boost both the photoelectrochemical activity, and operational stability, of the MBVO photoanodes. The promoted carrier transport in the shallow MBVO-V_O layer, and the efficient carrier extraction and band aligning in the LGCDs-PHGs layer, contribute greatly to the enhanced PEC activity, while the improved carrier dynamics in the dual interfacial layers and the uniform coating of top LGCDs-PHGs layer for suppressed photo-corrosion resulted in increased operational stability. The resulting LGCDs-PHGs-MBVO photoanode shows pronounced photocurrent density up to 6.08 mA cm^{-2} and a long-term operational stability of 120 h at 1.23 V_{RHE} in 1.0 M potassium phosphate buffer (pH = 7). Moreover, yielding such dual layers by grafting other laser generated carbon dots with functional groups was verified effective on the improved PEC

performance. This study could thus be beneficial in advancing the PEC water splitting through creating active SCLJ with synchronously boosted charge carrier dynamics, and kinetically suppressed photo-corrosion at surfaces of metal oxide photoelectrodes, based on laser-matter interactions.

Acknowledgements

This work was financially supported by the project of the National Natural Science Foundation of China (Nos. 51872240 and 51911530212), Shaanxi Province Key Research and Development Program (2021ZDLGY14-08), the Fundamental Research Funds for the Central Universities (3102019JC005), and the Joint Research Funds of Department of Science & Technology of Shaanxi Province and Northwestern Polytechnical University (2020GXLH-Z-018). The authors would like to thank the Analytical & Testing Center of Northwestern Polytechnical University and Shaanxi Materials Analysis and Research Center for ICP, XPS, SEM and TEM characterizations. Mr. Youxun Xu from University College London is acknowledged for his valuable discussion. DS, AN and VV acknowledge the support of the RSF project (project 19-79-30091) for funding this research.

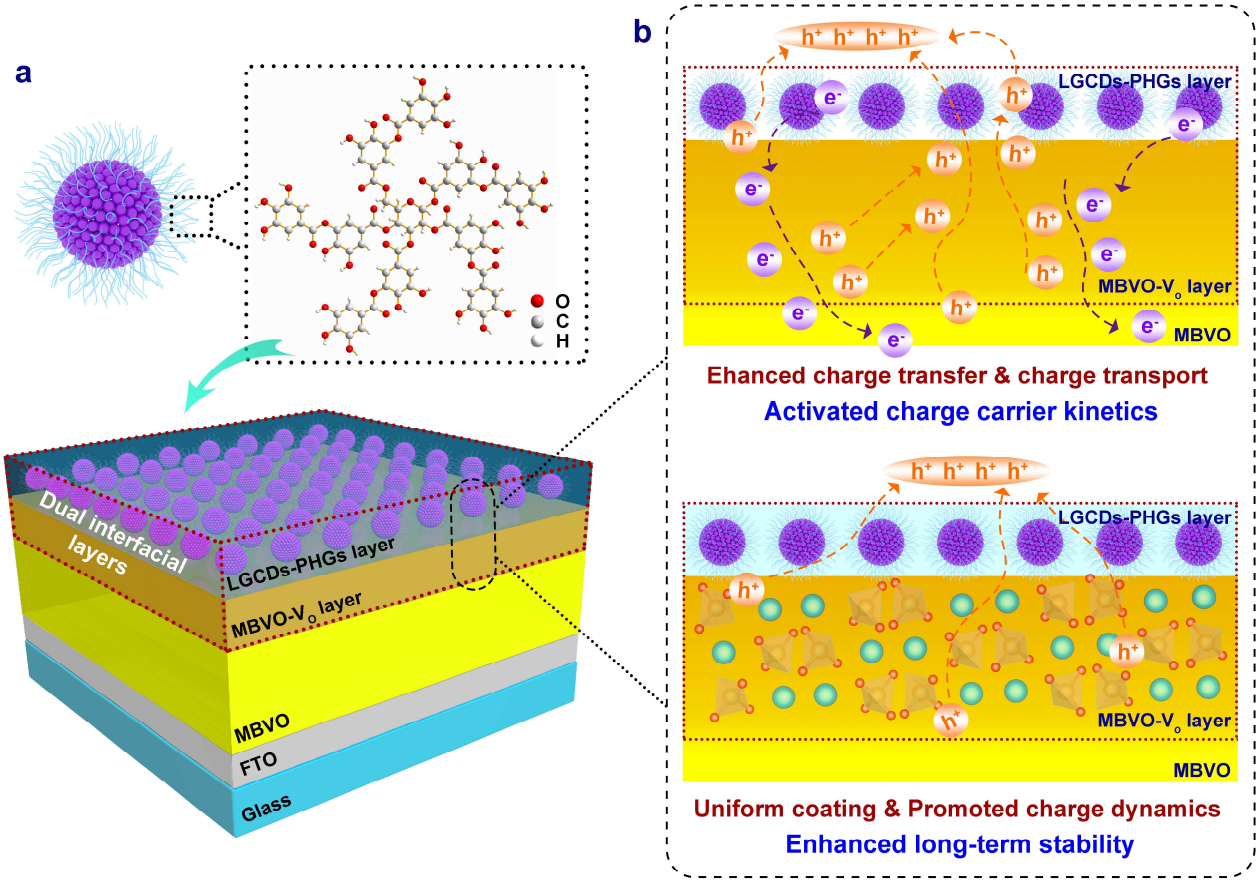

Scheme 1 (a) Schematic illustration of the dual interfacial layers at MBVO film. (**b**) Schematic illustration of the functions of dual interfacial layers for activated carrier dynamics and enhanced long-term stability.

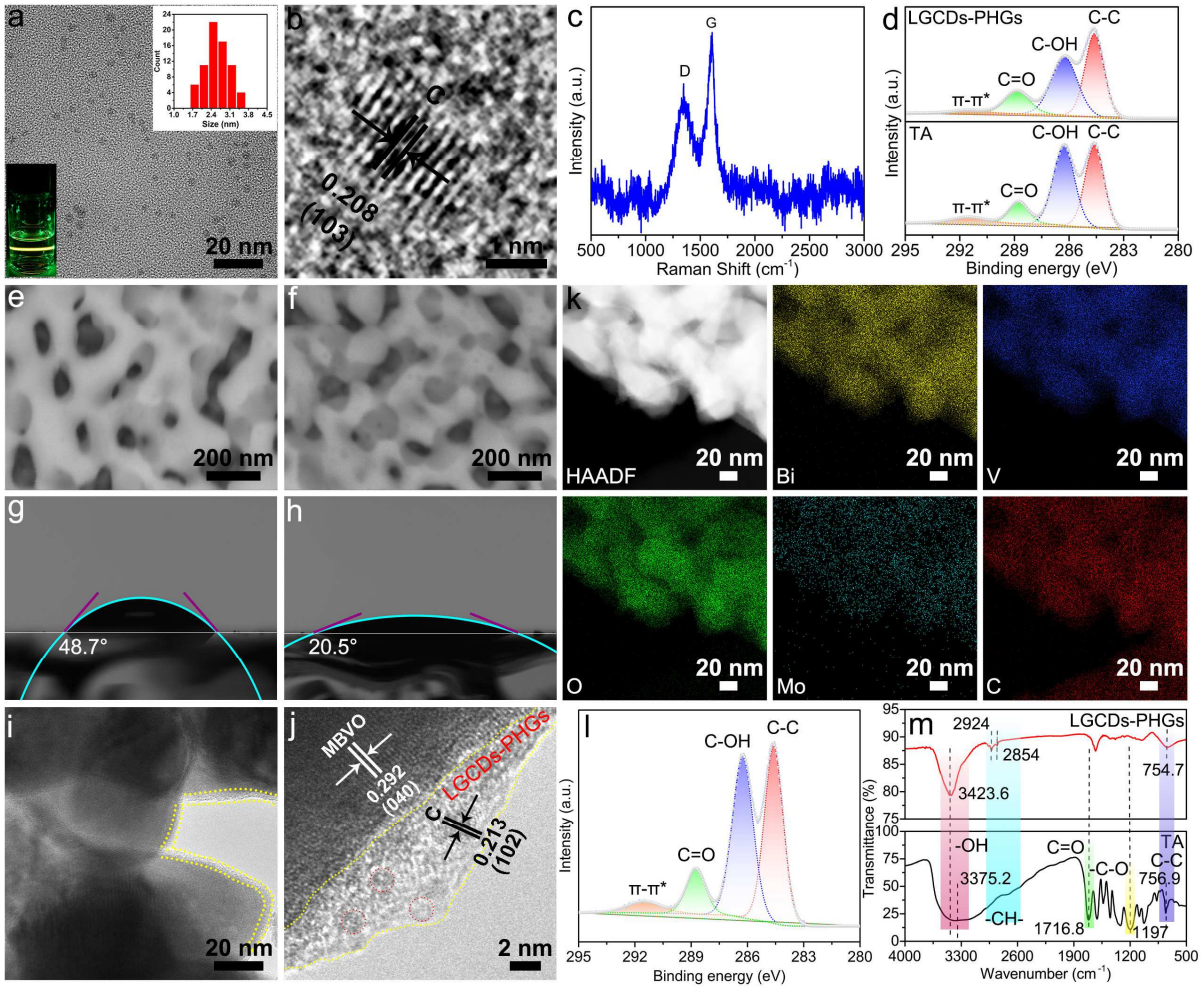

Figure 1 Characterizations of LGCDs-PHGs, MBVO and SCPHs-MBVO films. (a) TEM image of LGCDs-PHGs (inserts: Mie-scattering image of LGCDs-PHGs colloidal solution and size distribution of the LGCDs-PHGs). (**b**) HRTEM image of LGCDs-PHGs. (**c**) Raman spectra of the LGCDS-PHGs. (**d**) XPS spectrum of C 1s peaks of TA and LGCDs-PHGs. (**e**) BSE top-view image of MBVO film. (**f**) BSE top-view image of LGCDs-PHGs-MBVO film. (**g**) Contact angle of MBVO film. (**h**) Contact angle of LGCDs-PHGs-MBVO film. (**i**) TEM image of LGCDs-PHGs-MBVO film. (**j**) HRTEM image of LGCDs-PHGs-MBVO film. (**k**) TEM-EDS analysis of LGCDs-PHGs-MBVO film. (**l**) XPS spectrum of C 1s peaks of MBVO and LGCDs-PHGs-MBVO films. (**m**) FTIR spectrum of TA and LGCDs-PHGs-MBVO film.

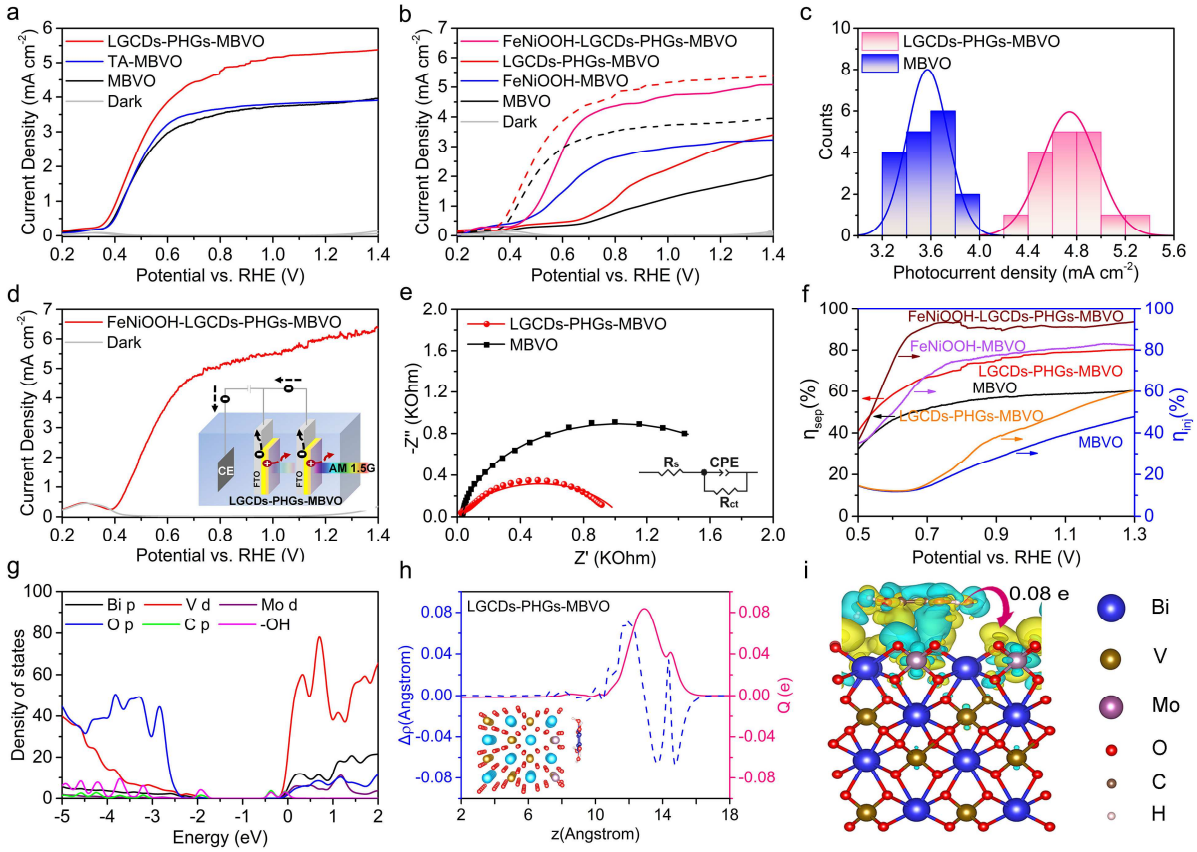

Figure 2 PEC Performance of MBVO and LGCDs-PHGs-MBVO films. (**a**) J–V curves of different MBVO based photoanodes in 1.0 M potassium phosphate buffer (pH = 7) with Na_2SO_3 under AM 1.5G irradiation. (**b**) J–V curves of various photoanodes in 1.0 M potassium phosphate buffer (pH = 7) with (dashed) and without (solid) Na_2SO_3 under AM 1.5G irradiation. (**c**) Photocurrent density distribution of MBVO and LGCDs-PHGs-MBVO films at 1.23 V_{RHE}. (**d**) J–V curve of LGCDs-PHGs-MBVO-Double photoanodes in 1.0 M potassium phosphate buffer (pH = 7) under AM 1.5G irradiation. (**e**) EIS curves of MBVO and LGCDs-PHGs-MBVO photoanodes. (**f**) Charge separation and injection efficiencies of MBVO and LGCDs-PHGs-MBVO photoanodes. (**g**) Partial density of states of LGCDs-PHGs-MBVO. (**h**) Adsorption-induced electron density redistribution integrated over the x−y plane (Δρ) (left panel) and the resulting total charge transfer (Q) (right panel) for the LGCDs-PHGs-MBVO systems as a function of z-coordinate. (**i**) Side view of the electron density difference of LGCDs-PHGs-MBVO at equilibrium distances.

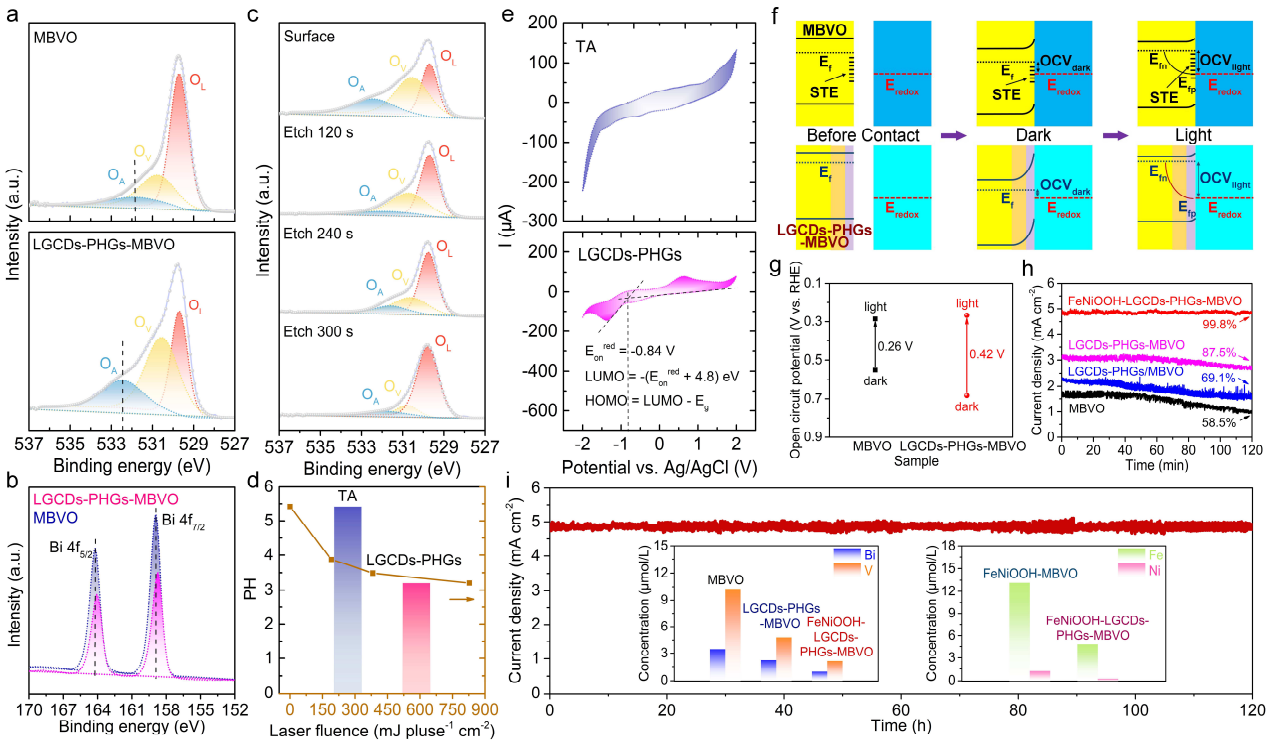

Figure 3 (**a**) XPS spectrum of O 1s peaks of MBVO and LGCDs-PHGs-MBVO films. (**b**) XPS spectrum of Bi 4f ($4f_{5/2}$ and $4f_{7/2}$) peaks of MBVO and LGCDs-PHGs-MBVO films. (**c**) Depth profile characterization of O 1s of LGCDs-PHGs-MBVO films. (**d**) PH analysis of different LGCDs-PHGs colloid solutions. (**e**) Cyclic voltammetry scans for TA and LGCDs-PHGs. (**f**) Band bending schematics of MBVO and LGCDs-PHGs-MBVO (STE: Surface trapped electrons). (**g**) Open-circuit potential of MBVO and LGCDs-PHGs-MBVO. (**h**) Photocurrent density stability of MBVO, LGCDs-PHGs/MBVO, LGCDs-PHGs-MBVO and FeNiOOH-LGCDs-PHGs-MBVO films. (**i**) Long-term stability of the FeNiOOH-LGCDs-PHGs-MBVO photoanode at 1.23 V_{RHE} (insert: ICP analysis of different potassium phosphate buffer after stability measurement).

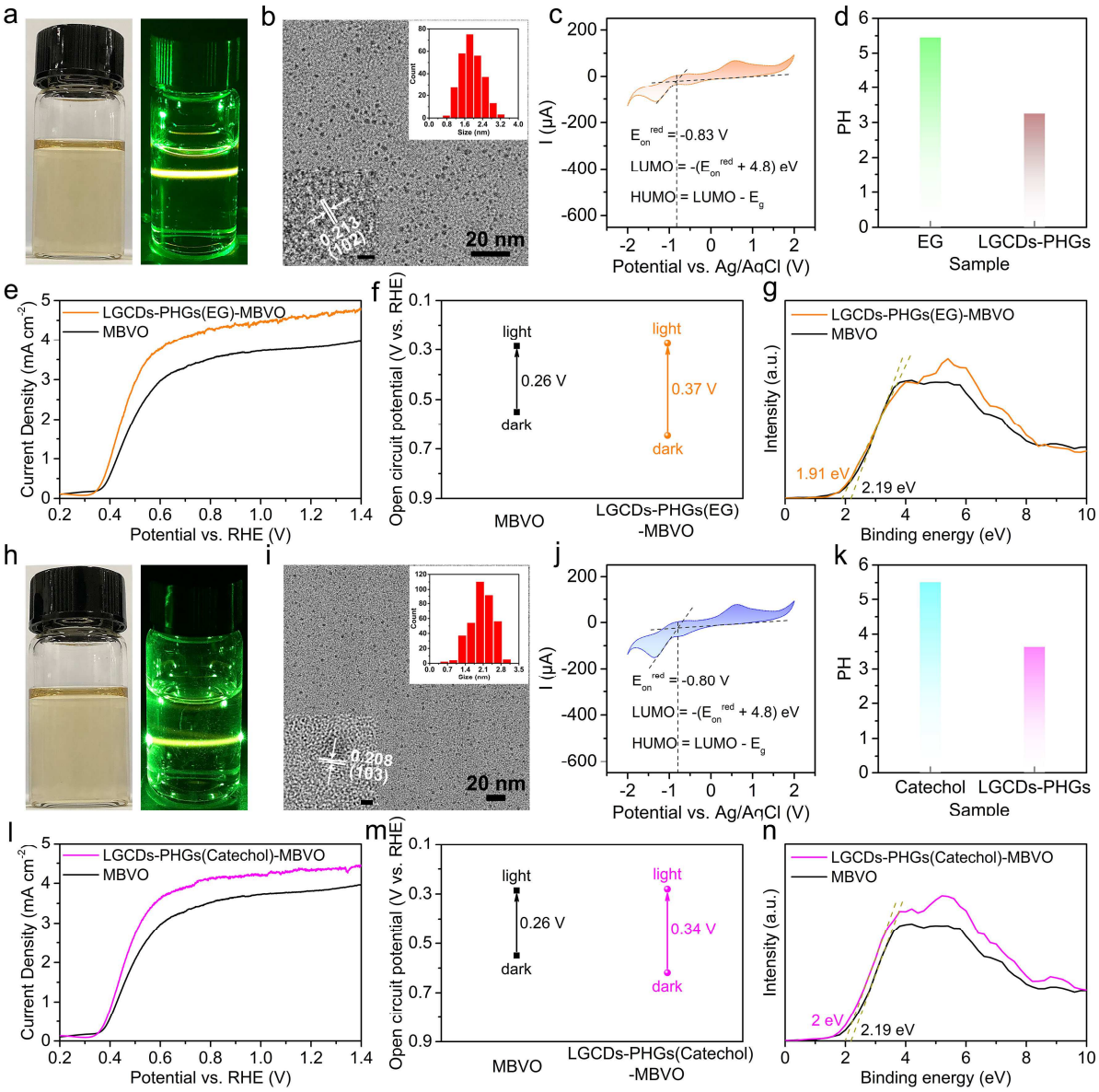

Figure 4. Characterizations of laser generated LGCDs-PHGs from EG and Catechol and the improved PEC performance of LGCDs-PHGs-MBVO films. Optical and Mie-scattering images of laser generated colloidal solution of (**a**) LGCDs-PHGs(EG) and (**h**) LGCDs-PHGs(Catechol). TEM image of (**b**) LGCDs-PHGs(EG) and (**i**) LGCDs-PHGs(Catechol) (inserts: HRTEM image and size distribution, scale bar: 1 nm). Cyclic voltammetry scans for (**c**) LGCDs-PHGs(EG) and (**j**) LGCDs-PHGs(Catechol). PH analysis of (**d**) LGCDs-PHGs(EG) and (**k**) LGCDs-PHGs(Catechol) colloid solutions. J–V curves of (**e**) LGCDs-PHGs(EG)-MBVO and (**l**) LGCDs-PHGs(Catechol)-MBVO photoanodes in 1.0 M potassium phosphate buffer (pH = 7) with Na_2SO_3 under AM 1.5G irradiation. Open-circuit potential of (**f**) LGCDs-PHGs(EG)-MBVO and (**m**) LGCDs-PHGs(Catechol)-MBVO. VB XPS of (**g**) LGCDs-PHGs(EG)-MBVO and (**n**) LGCDs-PHGs(Catechol)-MBVO photoanodes.

References

[1] Michael G. Walter, Emily L. Warren, James R. McKone, Shannon W. Boettcher, Qixi Mi, Elizabeth A. Santori, Nathan S. Lewis. Solar water splitting cells. Chem. Rev. 2010, 110, 6446-6473.

[2] Jinlong Gong, Can Li, Michael R. Wasielewski. Advances in solar energy conversion. Chem. Soc. Rev. 2019, 48, 1862.

[3] Kevin Sivula, Roel van de Krol. Semiconducting materials for photoelectrochemical energy conversion. Nat. Rev. Mater. 2016, 1, 15010.

[4] Jie Jian, Guangshen Jiang, Roel van de Krol, Bingqing Wei, Hongqiang Wang. Recent advances in rational engineering of multinary semiconductors for photoelectrochemical hydrogen generation. Nano Energy 2018, 51, 457-480.

[5] Dong Ki Lee, Dongho Lee, Margaret A. Lumley, Kyoung-Shin Choi. Progress on ternary oxide-based photoanodes for use in photoelectrochemical cells for solar water splitting. Chem. Soc. Rev. 2019, 48, 2126.

[6] Margaret A. Lumley, Andjela Radmilovic, Youn Jeong Jang, Ann E. Lindberg, Kyoung-Shin Choi. Perspectives on the development of oxide-based photocathodes for solar fuel production. J. Am. Chem. Soc. 2019, 141, 46, 18358-18369.

[7] Aron Walsh, Yanfa Yan, Muhammad N. Huda, Mowafak M. Al-Jassim, Su-Huai Wei. Band edge electronic structure of $BiVO_4$: elucidating the role of the Bi s and V d orbitals. Chem. Mater. 2009, 21, 547-551.

[8] Fatwa F. Abdi, Tom J. Savenije, Matthias M. May, Bernard Dam, Roel van de Krol. The origin of slow carrier transport in $BiVO_4$ thin film photoanodes: A time-resolved microwave conductivity study. J. Phys. Chem. Lett. 2013, 4, 2752-2757.

[9] Kenneth J. McDonald, Kyoung-Shin Choi. A new electrochemical synthesis route for a BiOI electrode and its conversion to a highly efficient porous $BiVO_4$ photoanode for solar water oxidation. Energy Environ. Sci. 2012, 5, 8553-8557.

[10] Chang Woo Kim, Young Seok Son, Myung Jong Kang, Do Yoon Kim, Young Soo Kang. (040)-crystal facet engineering of $BiVO_4$ plate photoanodes for solar fuel production. Adv. Energy Mater. 2016, 6, 1501754.

[11] Segi Byun, Gihun Jung, Song-Yi Moon, Bumsoo Kim, Jeong Young Park, Seokwoo Jeon, Sung-Wook Namd, Byungha Shin. Compositional engineering of solution-processed $BiVO_4$ photoanodes toward highly efficient photoelectronchemical water oxidation. Nano Energy 2018, 43, 244-252.

[12] Songcan Wang, Tianwei He, Peng Chen, Aijun Du, Kostya (Ken) Ostrikov, Wei Huang, Lianzhou Wang. In situ formation of oxygen vacancies achieving near-complete charge separation in planar

$BiVO_4$ photoanodes. Adv. Mater. 2020, 32, 2001385.

[13] Fatwa F. Abdi, Lihao Han, Arno H.M. Smets, Miro Zeman, Bernard Dam, Roel van de Krol. Efficient solar water splitting by enhanced charge separation in a bismuth vanadate-silicon tandem photoelectrode. Nat. Commun. 2013, 4, 2195.

[14] Jie Jian, Youxun Xu, Xiaokun Yang, Wei Liu, Maosen Fu, Huiwu Yu, Fei Xu, Fan Feng, Lichao Jia, Dennis Friedrich, Roel van de Krol, Hongqiang Wang. Embedding laser generated nanocrystals in $BiVO_4$ photoanode for efficient photoelectrochemical water splitting. Nat. Commun. 2019, 10, 2609.

[15] Miao Zhong, Takashi Hisatomi, Yongbo Kuang, Jiao Zhao, Min Liu, Akihide Iwase, Qingxin Jia, Hiroshi Nishiyama, Tsutomu Minegishi, Mamiko Nakabayashi, Naoya Shibata, Ryo Niishiro, Chisato Katayama, Hidetaka Shibano, Masao Katayama, Akihiko Kudo, Taro Yamada, Kazunari Domen. Surface modification of CoO_x loaded $BiVO_4$ photoanodes with ultrathin p-Type NiO layers for improved solar water oxidation. J. Am. Chem. Soc. 2015, 137, 5053-5060.

[16] Kai-Hang Ye, Haibo Li, Duan Huang, Shuang Xiao, Weitao Qiu, Mingyang Li, Yuwen Hu, Wenjie Mai, Hongbing Ji, Shihe Yang. Enhancing photoelectrochemical water splitting by combining work function tuning and heterojunction engineering. Nat. Commun. 2019, 10, 3687.

[17] Chunmei Ding, Jingying Shi, Zhiliang Wang, Can Li. Photoelectrocatalytic water splitting: significance of cocatalysts, electrolyte, and interfaces. ACS Catal. 2017, 7, 675-688.

[18] Rui Gao, Dongpeng Yan. Recent development of Ni/Fe-based micro/nanostructures toward photo/electrochemical water oxidation. Adv. Energy Mater. 2020, 10, 1900954.

[19] Diane K. Zhong, Sujung Choi, and Daniel R. Gamelin. Near-complete suppression of surface recombination in solar photoelectrolysis by "Co-Pi" catalyst-modified W:$BiVO_4$. J. Am. Chem. Soc. 2011, 133, 18370–18377.

[20] Tae Woo Kim, Kyoung-Shin Choi. Nanoporous $BiVO_4$ photoanodes with dual-layer oxygen evolution catalysts for solar water splitting. Science 2014, 343, 990-994.

[21] Yongbo Kuang, Qingxin Jia, Guijun Ma, Takashi Hisatomi, Tsutomu Minegishi, Hiroshi Nishiyama, Mamiko Nakabayashi, Naoya Shibata, Taro Yamada, Akihiko Kudo, Kazunari Domen. Ultrastable low-bias water splitting photoanodes via photocorrosion inhibition and in situ catalyst regeneration. Nat. Energy 2017, 2, 16191.

[22] Xiaoxia Chang, Tuo Wang, Peng Zhang, Jijie Zhang, Ang Li, Jinlong Gong. Enhanced surface reaction kinetics and charge separation of p-n heterojunction Co_3O_4/$BiVO_4$ photoanodes. J. Am. Chem. Soc. 2015, 137, 8356-8359.

[23] Mingshan Zhu, Zhichao Sun, Mamoru Fujitsuka, Tetsuro Majima. Z-scheme photocatalytic overall pure-water splitting on 2D heterostructure of black phosphorus/$BiVO_4$ using visible light. Angew. Chem. Int. Ed. 2018, 57, 2160-2164.

[24] Kan Zhang, Bingjun Jin, Cheolwoo Park, Yoonjun Cho, Xiufeng Song, Xinjian Shi, Shengli Zhang, Wooyul Kim, Haibo Zeng, Jong Hyeok Park. Black phosphorene as a hole extraction layer boosting solar water splitting of oxygen evolution catalysts. Nat. Commun. 2019, 10, 2001.

[25] Dejian Yan, Xingchen Fu, Zhichao Shang, Jikai Liu, He'an Luo. A $BiVO_4$ film photoanode with re-annealing treatment and 2D thin $Ti_3C_2T_X$ flakes decoration for enhanced photoelectrochemical water oxidation. Chem. Eng. J. 2019, 361, 853-861.

[26] Kai-Hang Ye, Zilong Wang, Jiuwang Gu, Shuang Xiao, Yufei Yuan, Yi Zhu, Yuanming Zhang, Wenjie Mai, Shihe Yang. Carbon quantum dots as a visible light sensitizer to significantly increase the solar water splitting performance of bismuth vanadate photoanodes. Energy Environ. Sci. 2017, 10, 772-779.

[27] Pengfei Guo, Xiaokun Yang, Qian Ye, Jin Zhang, Hongyue Wang, Huiwu Yu, Wenhao Zhao, Chen Liu, He Yang, Hongqiang Wang. Laser-generated nanocrystals in perovskite: universal embedding of ligand-free and sub-10 nm nanocrystals in solution-processed metal halide perovskite films for effectively modulated optoelectronic performance. Adv. Energy Mater. 2019, 9, 1901341.

[28] Xiaosa Xu, Youxun Xu, Fei Xu, Guangshen Jiang, Jie Jian, Huiwu Yu, Enming Zhang, Dmitry Shchukin, Stefan Kaskel, Hongqiang Wang. Black $BiVO_4$: size tailored synthesis, rich oxygen vacancies, and sodium storage performance. J. Mater. Chem. A, 2020, 8, 1636-1645.

[29] Jung Kyu Kim, Yoonjun Cho, Myung Jin Jeong, Ben Levy-Wendt, Dongguen Shin, Yeonjin Yi, Dong Hwan Wang, Xiaolin Zheng, Jong Hyeok Park. Rapid formation of a disordered layer on monoclinic $BiVO_4$: cocatalyst-free photoelectrochemical solar water splitting. ChemSusChem 2018, 11, 933-940.

[30] Zhangliu Tian, Pengfei Zhang, Peng Qin, Du Sun, Shaoning Zhang, Xiaowei Guo, Wei Zhao, Dongyuan Zhao, Fuqiang Huang. Novel black $BiVO_4/TiO_{2-x}$ photoanode with enhanced photon absorption and charge separation for efficient and stable solar water splitting. Adv. Energy Mater. 2019, 9, 1901287.

[31] Shijia Feng, Tuo Wang, Bin Liu, Congling Hu, Lulu Li, Zhi-Jian Zhao, Jinlong Gong. Enriched surface oxygen vacancies of photoanodes by photoetching with enhanced charge separation. Angew. Chem. Int. Ed. 2020, 59, 2044-2048.

[32] Rui-Ting Gao, Lei Wang. Stable cocatalyst-free $BiVO_4$ photoanodes with passivated surface states for photocorrosion inhibition. Angew. Chem. 2020, 132, 23294-23299.

[33] Dongshi Zhang, Bilal Gökce, Stephan Barcikowski. Laser synthesis and processing of colloids: fundamentals and applications. Chem. Rev. 2017, 117, 3990-4103.

[34] Hongqiang Wang, Alexander Pyatenko, Kenji Kawaguchi, Xiangyou Li, Zaneta Swiatkowska-Warkocka, Naoto Koshizaki. Selective pulsed heating for the synthesis of semiconductor and

metal submicrometer spheres. Angew. Chem. 2010, 122, 6505-6508.

[35] Hongqiang Wang, Masahiro Miyauchi, Yoshie Ishikawa, Alexander Pyatenko, Naoto Koshizaki, Yue Li, Liang Li, Xiangyou Li, Yoshio Bando, Dmitri Golberg. Single-crystalline rutile TiO_2 hollow spheres: room-temperature synthesis, tailored visible-light-extinction, and effective scattering layer for quantum dot-sensitized solar cells. J. Am. Chem. Soc. 2011, 133, 19102-19109.

[36] Hongqiang Wang, Naoto Koshizaki, Liang Li, Lichao Jia, Kenji Kawaguchi, Xiangyou Li, Alexander Pyatenko, Zaneta Swiatkowska-Warkocka, Yoshio Bando, Dmitri Golberg. Size-tailored ZnO submicrometer spheres: bottom-up construction, size-related optical extinction, and selective aniline trapping. Adv. Mater. 2011, 23, 1865-1870.

[37] Takuya Okamoto, Koji Mitamura, Tomoyuki Hamaguchi, Kimihiro Matsukawa, Tomoyuki Yatsuhashi. Synthesis of fluorine-doped hydrophilic carbon nanoparticles from hexafluorobenzene by femtosecond laser pulses. ChemPhysChem 2017, 18, 1007-1011.

[38] Aldo Ponce, Lynn B. Brostoff, Sarah K. Gibbons, Peter Zavalij, Carol Viragh, Joseph Hooper, Sufian Alnemrat, Karen J. Gaskell, Bryan Eichhorn. Elucidation of the Fe(III) gallate structure in historical iron gall ink. Anal. Chem. 2016, 88, 5152-5158.

[39] Sebastian Geißler, Alejandro Barrantes, Pentti Tengvall, Phillip B. Messersmith, Hanna Tiainen. Deposition kinetics of bioinspired phenolic coatings on titanium surfaces. Langmuir 2016, 32, 8050-8060.

[40] Hirotaka Ejima, Joseph J. Richardson, Kang Liang, James P. Best, Martin P. van Koeverden, Georgina K. Such, Jiwei Cui, Frank Caruso. One-step assembly of coordination complexes for versatile film and particle engineering. Science 2013, 341, 154-157.

[41] Qian Ye, Feng Zhou, Weimin Liu. Bioinspired catecholic chemistry for surface modification. Chem. Soc. Rev. 2011, 40, 4244-4258.

[42] Yanmei Shi, Yifu Yu, Yu Yu, Yi Huang, Bohang Zhao, Bin Zhang. Boosting photoelectrochemical water oxidation activity and stability of Mo-doped $BiVO_4$ through the uniform assembly coating of NiFe-phenolic networks. ACS Energy Lett. 2018, 3, 1648-1654.

[43] Andriana Surleva, Petya Atanasova, Tinka Kolusheva, Latinka Costadinnova. Study of the complex equilibrium between titanium (IV) and tannic acid. J. Chem. Technol. Metall. 2014, 49, 594-600.

[44] Cho J, Roy S, Sathyapalan A, Free LM, Fang ZZ. Tannic acid selectively extracting titanium from ilmenite: experimental and theoretical investigation. J. Powder Metall. Min. 2017, 6, 1000183.

[45] Mayra A. Pantoja-Castro, Horacio González-Rodríguez. Study by infrared spectroscopy and thermogravimetric analysis of tannins and tannic acid. Rev. Latinoam. Quím. 2011, 39, 107-112.

[46] Huiwu Yu, Xiangyou Li, Xiaoyan Zeng, Yongfeng Lu. Preparation of carbon dots by non-focusing pulsed laser irradiation in toluene. Chem. Commun. 2016, 52, 819-822.

[47] Benjamin Klahr, Sixto Gimenez, Francisco Fabregat-Santiago, Thomas Hamann, Juan Bisquert. Water oxidation at hematite photoelectrodes: The role of surface states. J. Am. Chem. Soc. 2012, 134, 4294-4302.

[48] Songcan Wang, Peng Chen, Yang Bai, Jung-Ho Yun, Gang Liu, Lianzhou Wang. New $BiVO_4$ dual photoanodes with enriched oxygen vacancies for efficient solar-driven water splitting. Adv. Mater. 2018, 30, 1800486.

[49] Jason K. Cooper, Sheraz Gul, Francesca M. Toma, Le Chen, Per-Anders Glans, Jinghua Guo, Joel W. Ager, Junko Yano, Ian D. Sharp. Electronic structure of monoclinic $BiVO_4$. Chem. Mater. 2014, 26, 5365-5373.

[50] Guirong Su, Sha Yang, Shuang Li, Christopher J. Butch, Sergey N. Filimonov, Ji-Chang Ren, Wei Liu. Switchable schottky contacts: simultaneously enhanced output current and reduced leakage current. J. Am. Chem. Soc. 2019, 141, 1628-1635.

[51] Tae Woo Kim, Yuan Ping, Giulia A. Galli, Kyoung-Shin Choi. Simultaneous enhancements in photon absorption and charge transport of bismuth vanadate photoanodes for solar water splitting. Nat. Commun. 2015, 6, 8769.

[52] Qijun Meng, Biaobiao Zhang, Lizhou Fan, Haidong Liu, Mario Valvo, Kristina Edström, Maria Cuartero, Roland de Marco, Gaston A. Crespo, Licheng Sun. Efficient $BiVO_4$ photoanodes by postsynthetic treatment: remarkable improvements in photoelectrochemical performance from facile borate modification. Angew. Chem. Int. Ed. 2019, 58, 19027-19033.

[53] Gongming Wang, Yichuan Ling, Xihong Lu, Fang Qian, Yexiang Tong, Jin Z. Zhang, Vincenzo Lordi, Cedric Rocha Leao, Yat Li. Computational and photoelectrochemical study of hydrogenated bismuth vanadate. J. Phys. Chem. C 2013, 117, 10957-10964.

[54] Zhenghui Luo, Fei Wu, Teng Zhang, Xuan Zeng, Yiqun Xiao, Tao Liu, Cheng Zhong, Xinhui Lu, Linna Zhu, Shihe Yang, Chuluo Yang. Designing a perylene diimide/fullerene hybrid as effective electron transporting material in inverted perovskite solar cells with enhanced efficiency and stability. Angew. Chem. Int. Ed. 2019, 58, 8520-5825.

[55] Vikash Kumar Ravi, Ganesh B. Markad, Angshuman Nag. Band edge energies and excitonic transition probabilities of colloidal $CsPbX_3$ (X = Cl, Br, I) perovskite nanocrystals. ACS Energy Lett. 2016, 1, 665-671.

[56] Yunchao Li, Haizheng Zhong, Rui Li, Yi Zhou, Chunhe Yang, Yongfang Li. High-yield fabrication and electrochemical characterization of tetrapodal CdSe, CdTe, and $CdSe_xTe_{1-x}$ nanocrystals. Adv. Funct. Mater. 2006, 16, 1705-1716.

[57] Feng Nan, Tianyi Cai, Sheng Ju, Liang Fang. Enhanced photoelectrochemical water splitting of

$BiVO_4$ photonic crystal photoanode by decorating with MoS_2 nanosheets. Appl. Phys. Lett. 2018, 112, 173902.

[58] Angang Song, Paul Plate, Abdelkrim Chemseddine, Fuxian Wang, Fatwa F. Abdi, Markus Wollgarten, Roel van de Krol, Sean P. Berglund. Cu:NiO as a hole-selective back contact to improve the photoelectrochemical performance of $CuBi_2O_4$ thin film photocathodes. J. Mater. Chem. A, 2019, 7, 9183-9194.

[59] Dong Ki Lee, Kyoung-Shin Choi. Enhancing long-term photostability of $BiVO_4$ photoanodes for solar water splitting by tuning electrolyte composition. Nat. Energy 2018, 3, 53.